AIAA 2014-0908
AIAA SciTech
13-17 January 2014, National Harbor, Maryland
52nd Aerospace Sciences Meeting

High-fidelity Aerodynamic Shape Optimization of Unconventional Aircraft through Axial Deformation

Hugo Gagnon* and David W. Zingg†
Institute for Aerospace Studies, University of Toronto, Toronto, Ontario, M3H 5T6, Canada

This paper assesses the potential of unconventional aircraft configurations for regional transport through high-fidelity aerodynamic shape optimization. Several configurations are investigated: a C-tip blended-wing-body, a box-wing, and a truss-braced wing concept, and compared against a conventional jet similar in features and mission to the Bombardier CRJ-1000. In all cases the objective is to minimize drag subject to lift and trim constraints using a gradient-based optimizer coupled with a solver for the Euler equations governing inviscid compressible flow. A novel parameterization technique derived from a combination of axial and free-form deformation tools enables both planform and sectional shape changes to the main lifting surfaces. The sensitivities of the aerodynamic functionals, e.g. lift and drag, to the design variables are calculated analytically through the discrete-adjoint method. Results point to the strut-braced wing as the most promising configuration with induced drag reduction on the order of 46% relative to the tube-wing baseline.

I. Introduction

The impact of aviation on the environment will soon become, if it is not already, the main driving factor affecting the design of future aircraft.[1] This is reflected by the establishment of numerous projects worldwide that share the same ultimate goal: to develop a greener aircraft industry. For instance, NASA's environmentally responsible aviation project[2] has set aggressive milestones for the 2015, 2020 and 2025 scenarios that are aimed mainly at noise, emissions and performance improvements. The present work is concerned with the last two of these three tactics, namely by minimizing drag produced by unconventional aircraft at cruise. For a set mission, improved performance leads to reduced emissions.

One of the most cited benefits of unconventional aircraft configurations is their potential to offer higher flight efficiencies through lower induced drag. Induced drag, also known as drag due to lift, is an inviscid phenomenon experienced by wing systems of finite span. It accounts for roughly 40% of the total drag on a conventional aircraft at cruise.[3] Early attempts at mitigating this form of drag include the work of Munk,[4] Mangler,[5] and Cone,[6] which led to all kinds of intriguing nonplanar shapes.[7] An example is the ring-wing; when optimally loaded, it has half the induced drag of an optimally loaded planar wing of the same span and lift.[4] Fundamental research later turned to drag at transonic speeds[8] and derivative technologies,[9] presumably due to their higher relevance to the commercial jet transports introduced at that time.

It seems that the incremental approach to drag reduction of the conventional tube-wing is reaching an asymptote; hence the renewed interest for novel configurations.[10] The ideas behind most futuristic designs are not new, only their applications are. The "best wing system" derived by Prandtl[11] led to Miranda's transonic "boxplane",[12] which was later refined by Frediani for a range of civil transports of varying capacity.[13] The blended-wing-body, whose origins can be traced back almost as far as the Wright brothers' flying machine, is reported by Liebeck to offer fuel burn per seat mile savings of 27% relative to an equivalent conventional baseline.[14] The truss-braced design of Pfenninger[15] inspired many; see, for example, Ref. 16 where it is studied in the context of a high-speed civil transport for minimum fuel.

Most configurations cited above have undergone trade studies to establish feasibility in various technological and market scenarios.[17–19] However, while the assessment of their aerodynamic performance through

*PhD Candidate and AIAA Student Member
†Professor and Director, Tier 1 Canada Research Chair in Computational Aerodynamics and Environmentally Friendly Aircraft Design, J. Armand Bombardier Foundation Chair in Aerospace Flight, AIAA Associate Fellow

computational fluid dynamics is common,[13,20] their refinement through high-fidelity aerodynamic shape optimization (ASO) is still rare. This is with the exception of the blended-wing-body, which recently has even seen aspects of high-fidelity multidisciplinary analysis and optimization (MDO) incorporated into its design cycle.[21–23] Still, there is a clear need for a unified study based on high-fidelity ASO that compares practical unconventional aircraft to a conventional baseline on the basis of environmental friendliness. One contributing factor for this apparent gap is the difficulty of generating high-quality surfaces suitable for such purposes.

All aircraft geometries investigated in this work were generated by a specialized in-house drawing tool that outputs outer mold lines in the form of smooth networks of nonuniform rational B-spline surfaces (NURBS).[24] They consist of a conventional tube-wing baseline aircraft, a C-tip blended-wing-body, a box-wing configuration, and a strut-braced wing configuration; all are regional jets sized for a nominal 100 passenger mission of 500 nm. In all cases, we minimize drag while maintaining trimmed lift at Mach 0.78, thus effectively maximizing cruising aerodynamic efficiency. While acknowledging their importance, we exclude all other considerations such as structures, stability, off-design performance, etc. Thus, we take a step back and ask: from a purely aerodynamic standpoint, how much is there to gain by deviating from the ubiquitous tube-wing? It is our hope that by including nonlinear effects as captured by the Euler equations we will observe subtle trends otherwise undetectable with commonly used lower fidelity models.[25,26]

Another difficulty with ASO at this level of geometric fidelity is the one of parameterization and deformation. A plethora of methods with varying degrees of success on airfoils and cantilever wings have been proposed in the past; see, for instance, Ref. 27 for an excellent review. Yet we found that none truly satisfied our needs; hence we developed and now present a novel parameterization scheme specifically tailored for wing systems of arbitrary topology. It can be regarded as an extension to our previous work on free-form deformation,[28] whereby both surface and volume grids are tightly integrated with the geometry. Our new approach is extremely intuitive and ideally suited for exploratory shape optimization, an important feature in the realm of unconventional aircraft.

The subsequent sections are divided as follows. In Section II we begin by formally presenting axial deformation before demonstrating its suitability for wing shape design. A quick overview of our state-of-the-art aerodynamic optimizer is given in Section III. In Section IV all four initial designs are then described along with the rationale behind their sizing, after which we carry out both twist-only span efficiency validations and practical drag minimizations subject to lift as well as trim constraints. Finally, Section V contains concluding remarks and future directions.

II. Axial Deformation Adapted for Arbitrary Wing Systems

When confronted with aerodynamic shape design, the aerospace engineer must first choose one of two geometry modeling paradigms: construction-based or deformation-based. The first route typically involves well-developed and well-documented CAD packages, but comes with equally heavy disadvantages.[29] For one, operating a high-end CAD interface requires great expertise. Due to the internal source tree geometry representation of CAD engines, the task of creating the right parametric "recipe" that shall ensure a thorough exploration of the design space at the optimization stage is a difficult one, even for an experienced operator. This is not to mention the proprietary rights protecting the large corporations responsible for the software, giving the designer very little to no freedom in accessing their source code, let alone modifying it.

Turning to deformation-based geometry modeling, we are again presented with two alternatives: surface-based or volume-based. The first usually involves analytic functions, such as Hicks-Henne bumps and Bézier polynomials, or some kind of variational method where for example a curvature norm is minimized. Not only does the latter option not scale well (matrix condition worsened with system size), but both surface-based approaches are ill-suited for 1) maintaining continuity across seams adjoining surface patches, and 2) simultaneously accommodating multiple cross-disciplinary geometry formats such as is the case in aerostructural problems. In contrast, volumetric deformation techniques, such free-form deformation[30] (FFD), provide embedded objects with smooth deformations, irrespective of their discipline and format.

If one is not careful, the attractive properties of FFD — intuitiveness, smoothness, local control, rapid deformation, mathematical background — can be quickly overshadowed by the overwhelming number of control points that an FFD lattice may require. This is a simple consequence of its tensor product definition. Ideally, a wing designer would be able to rely on FFD's excellent intrinsic properties, while being spared from the cumbersome task of constraining every individual control point to prevent unfeasible designs. The most

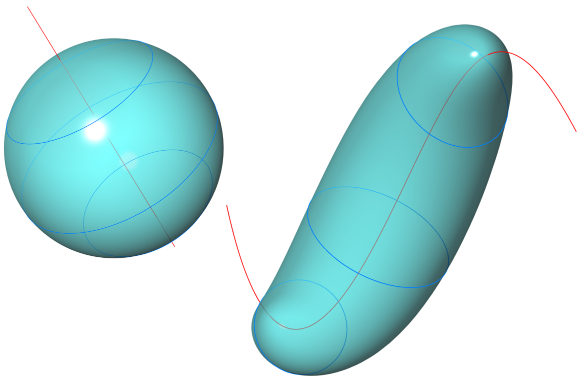

Figure 1: Axial deformation: a curve deforms an object in 3D space such that the cross sections of the object always remain perpendicular to the curve's local axes.

obvious way of achieving this is to group control points by proximity, and let a simpler, higher level object control the overall movement of the lattice. In this work, we investigate the use of axial curves for such purposes in the context of wing design. The result is a highly general and intuitive deformation technique that confines the design space to what makes sense aerodynamically, but without overly constraining possibly optimal wing shapes.

The term "axial deformation" was coined by Lazarus et al.[31] in 1994 and has since enjoyed some popularity, especially in the computer graphics community.[32] Like FFD, it is a volumetric deformation technique that, as its name suggests, operates from a single curve, i.e. the axial curve. Figure 1 shows the conceptual idea behind its functioning. First, an axial curve is positioned either inside or outside an object of interest. Once every point of that object has been associated (mapped) to the closest point on the axial curve, the axial curve is deformed, after which the initial points are re-evaluated to their new world space coordinates based on their new local coordinate frame. Although not shown in Figure 1, other effects such as twisting and scaling can be achieved by means of transformational functions.

The application to wing deformation follows directly. Refer to Figure 2 where the chordwise, spanwise, and vertical directions of the wing are assumed to be oriented along the positive $\mathbf{X}$, $\mathbf{Y}$, and $\mathbf{Z}$ directions, respectively.

Let the axial curve be a NURBS curve[33] defined with n control points $\mathbf{P}_i$ and n piecewise rational polynomials of degree p, $\mathcal{R}_i^{(p)}(u)$:

$$\mathbf{A}\,(u) = \sum_{i=1}^{n} \mathcal{R}_i^{(p)}(u)\,\mathbf{P}_i, \qquad 0 \leq u \leq 1. \tag{1}$$

The basis functions are joined at non-decreasing knot locations $\{u_i\}_{i=1}^{n+p+1}$, where the end knot multiplicities must equal the order of the splines in order for $\mathbf{A}(0)$ and $\mathbf{A}(1)$ to pass exactly through the end control points $\mathbf{P}_1$ and $\mathbf{P}_n$, respectively.

The first step is to position $\mathbf{A}(u)$ relative to the wing, for example at the wing's quarter-chord curve as shown in Figure 2. Next, relative to the global origin, $\mathbf{O}$, a local orthonormal coordinate system $\{\mathbf{o}(u), \mathbf{x}(u), \mathbf{y}(u), \mathbf{z}(u)\}$ that moves along $\mathbf{A}(u)$ is introduced. For any given $u \in [0, 1]$, let

$$\mathbf{o}(u) = \mathbf{A}(u), \qquad \mathbf{y}(u) = \frac{\mathbf{A}'(u)_\perp}{\|\mathbf{A}'(u)_\perp\|}, \tag{2}$$

where the prime denotes the first derivative in u and the $\perp$ symbol refers to the projected vector onto the $\mathbf{YZ}$ plane (the reason for this projection will be clarified below). We define wing twist to be about the axial curve, and compute $\mathbf{z}(u)$ directly from its spanwise distribution. Indeed, assuming $\mathbf{B}(u)$ to be a vector-valued function satisfying $\mathbf{B}(u) \cdot \mathbf{y}(u) = 0$ for all u, we have

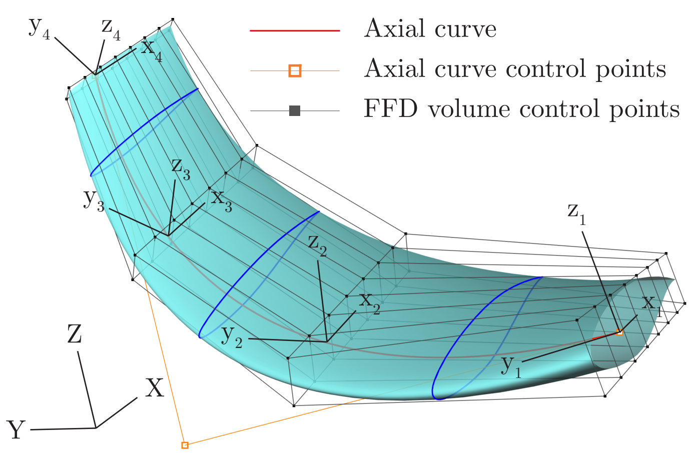

Figure 2: Axial-driven free-form deformation applied to a generic wing.

$$\mathbf{z}(u) = \frac{\mathbf{B}(u)}{\|\mathbf{B}(u)\|}. \tag{3}$$

Finally, $\mathbf{x}(u)$ is simply defined as

$$\mathbf{x}(u) = \mathbf{y}(u) \times \mathbf{z}(u). \tag{4}$$

For the special case of an untwisted wing, then $\mathbf{x}(u) = \mathbf{X}$ for all u (hence $\mathbf{y}(u)$ and $\mathbf{z}(u)$ appear perpendicular when looking in the $\mathbf{X}$ direction).

The next step is to enclose the wing inside a sufficiently large FFD lattice whose spanwise cross-sections are oriented according to the local coordinate functions described by Eqs. (2–4). Specifically, let $\bar{u}_1, \ldots, \bar{u}_m$ be the parameters associated with m such cross-sections; then the local coordinate system associated with the first one is $\{\mathbf{o}(\bar{u}_1), \mathbf{x}(\bar{u}_1), \mathbf{y}(\bar{u}_1), \mathbf{z}(\bar{u}_1)\}$, and so forth. Also notice, in Figure 2 (where $m = 4$), how control points pertaining to the same cross-section reside in the same plane perpendicular to the local $\mathbf{y}$ axis. This requirement, together with the projection of $\mathbf{y}(u)$ in Eq. 2, is required in order to keep wing cross-sections facing the flow field no matter what the orientation of $\mathbf{A}(u)$ becomes. Lastly, as for the degree selection of the FFD splines, we use cubic NURBS both in the chordwise and spanwise directions, but linear in the vertical direction. This choice forces the number of control points in the vertical direction to two, and to a minimum of four in the other two directions.

Once the FFD volume is setup, and each one of its spanwise lattice cross-sections "attached" to a point on the axial curve, the wing's surfaces are embedded (mapped) to the FFD volume (as apposed to the axial curve, as originally proposed by Lazarus). This is normally carried out by a Newton search procedure, and needs only be performed once. An important note here is that we embed the surfaces' control points rather than their discretizations. This allows us to integrate surface and volume mesh movement tightly for increased computational efficiency. More on this topic is given in the next section.

At this point the axial curve can be deformed, followed by the FFD lattice, and finally the embedded wing. Manipulating the axial curve's control points enables variations in span, sweep, and dihedral. To vary twist, chord, and sectional shape, a sequence of transformation matrices[34,35] can be applied separately to each FFD cross-section. For example, let $\mathsf{S}(Q, c, w)$ be a scaling operator where Q is the scaling origin, c the scaling factor, and w the scaling direction; then $\mathsf{S}(\mathbf{o}(\bar{u}_1), x, \mathbf{z}(\bar{u}_1))$ scales an FFD control point pertaining to the first cross-section by a factor of x in the local vertical direction, thus impacting the wing's sectional shape within the region of influence of that control point. Because other transformations are similarly taken about the local origins $\{\mathbf{o}(\bar{u}_i)\}_{i=1}^{m}$, it should be clear that the position of the axial curve relative to the wing matters; if say, twist about the trailing edge is desired then the axial curve should be positioned accordingly.

By judiciously choosing the number and placement of control points of both the axial curve and attached FFD volume, as well as their degree, it is possible to achieve any combination of linear or nonlinear variations in span, sweep, dihedral, twist, chord, and sectional shape. We also emphasize the fact that the sole purpose of the axial curve is to "drive" the movement of the FFD volume, and as such both entities are completely decoupled insofar as their mathematical definitions go. This is desirable, for example, in cases where more FFD cross-sections are required for increased local surface control but without the typical increase in number of planform design variables.

III. Discrete Adjoint-Based Aerodynamic Optimizer

The axial deformation scheme just introduced is part of a broader ASO methodology developed by the University of Toronto Computational Aerodynamics Group. The core components of the methodology are thoroughly described and verified in Ref. 36; thus only a brief summary is given here.

Following an update in the design variables, e.g. the xyz-coordinates of axial control points, wing sections are regenerated by updating the location of the embedded surface control points. To account for these changes inside the computational domain, we initially fit our multi-block grids with as many FFD volumes as there are blocks[a], and we make sure that the FFD control points bordering the geometry fall exactly on the embedded control points of the wings. This allows us to apply the equations of linear elasticity to this much coarser grid of FFD control points and to subsequently regenerate the computational mesh algebraically. This semi-algebraic method results in fast, high-quality mesh movements and is robust enough to accommodate very large shape changes.[28,36]

With the computational mesh conforming to the deformed geometry, the aerodynamic functionals are then evaluated based on the solution of the Euler governing equations. Those are discretized with second-order accurate finite-difference summation-by-parts operators.[37] Simultaneous approximation terms[38] are applied to enforce boundary conditions and couple blocks, requiring only C^0 continuity between matching mesh lines at interfaces. The solution in the vicinity of shocks is stabilized by a pressure switch mechanism involving both second- and fourth-difference scalar dissipation. Further details regarding the flow solver are

[a] This second level of FFD volumes is completely separate from those of the axial-driven FFD, see Ref. 28.

available in Ref. 39.

We use the gradient-based optimization package SNOPT[40] to find locally optimal designs. SNOPT is based on sequential quadratic programming, where the Hessian of the Lagrangian is approximated using the quasi-Newton method of Broyden, Fletcher, Goldfarb, and Shanno.[41] SNOPT is capable of handling problems with large numbers of design variables and constraints, as long as all gradient entries are provided by the user[b]. For aerodynamic functionals, which depend on the flow, the gradients are calculated analytically by using discrete-adjoint variables.[36] Other constraints, such as projected area and volume, are mostly hand-differentiated. In all cases the sensitivity of the surface control points to the axial design variables are computed to machine accuracy with the complex-step method.[42]

IV. Applications to Unconventional Aircraft

One of the main attractive features of high-fidelity numerical ASO is that, once a problem is properly setup and launched, it supersedes human intuition. This strength becomes even more powerful when such tools are applied to unconventional aircraft, for which very little empirical knowledge exists. The goal of this section is to demonstrate such capabilities by minimizing the sum of induced and wave drag components of three different aircraft configurations subject to lift and trim constraints, and comparing them against a similarly optimized conventional baseline aircraft (Figure 3). In order to give the reader enough confidence in our newly proposed axial deformation scheme, we present validation test cases based on span efficiencies before including practical constraints.

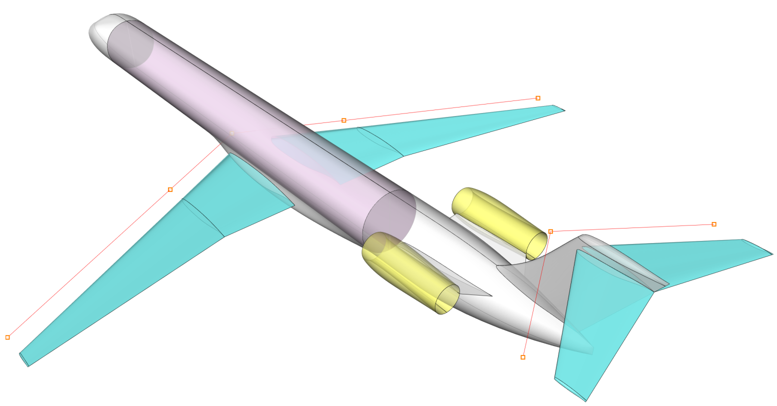

Figure 3: Conventional tube-wing regional jet. The axial curves are shown in red and their control points in orange.

Similar to the Bombardier CRJ-1000 NextGen, the configurations considered herein are aimed at the medium-haul 100-passenger market segment. Their planform is borrowed (or heavily inspired) from already existing concepts that we scale to ensure that their fuselage contains enough room to house the passenger compartment, visible in magenta in Figures 3 to 6. Note that the fuselages and propulsion systems shown on these figures are not included in the flow analyses of the ASO problems, although their weights are considered for the designs presented in Section B. Refer to Appendix A where 3-views of all four initial jets are pictured along with some core dimensions. The corresponding wetted areas are given in Table 1.

We select the wing sections based on a mix of historical trends, as described in the book of Raymer,[43] and two-dimensional methods. Specifically, starting from a rough aircraft weight estimate and a fixed planform, we iteratively interpolate wing segments with airfoils taken from NASA's supercritical phase 2 study[44] until the desired theoretical lift is achieved. This gives reasonable initial estimates since the reported design lift coefficients of NASA's airfoils assume zero angle-of-attack, which we match during the optimizations. Moreover, we fix the far field Mach number to 0.78, in agreement with the reported cruising speed of the actual CRJ-1000.[45]

The baseline tube-wing pictured in Figure 3 is modeled to the best of our ability from what is publicly

[b] Strictly speaking, this requirement is optional since SNOPT can finite-difference them; however this would not only be prohibitive but would also yield values subject to round-off and truncation errors.

Conventional tube-wing	C-tip blended-wing-body	Box-wing	Strut-braced wing
472.12	475.79	544.75	560.66

Table 1: Total aircraft wetted area [m^2].

available on the CRJ-1000. The pressurized cabin is designed for a 2-2 seating arrangement and long enough to seat 104 passengers in economy class. Rather than trying to replicate the exact winglet (which is taken from the CRJ-900, which is itself a scaled version of the one found on the CRJ-700), we choose not to model any on the initial geometry but, as discussed in Section B, we give the optimizer enough freedom to produce one on its own. The main wing is essentially a scaled-up version of the CRJ-700 W34 planform:[46] straight leading edge swept back 30 degrees with a root plug ending at 35% span. Based on the airfoil selection design process described above, we opt for the NASA SC(2)-0614, -0412, and -0410 at the root, kink, and tip sections, respectively. This choice yields satisfactory lift coefficients at the expense of small wave drag penalties.

The blended-wing-body studied in this work, Figure 4, is based on the released press on the X-48C hybrid/blended-wing-body demonstrator. Unlike the X-48C, it features C-tip extensions on the outboard wings, which provide directional control and stability on top of mitigating induced drag. The nose bullet, intended for increased cockpit visibility, somewhat complicates surface generation. Indeed, the challenging task of fitting the necessary volume inside a compact yet smooth blended-wing-body of this size might very well explain its usual application to very large transports. Here, a 2-4-2 cabin layout is assumed for improved ride quality, with the cargo bays and fuel tanks located outboard. An airfoil stack arising from the linear interpolation of a (modified) NASA SC(2)-0010 airfoil at the root and an (unmodified) NASA SC(2)-0410 airfoil at the tip is fitted in a single sweep to generate a C^2 continuous outer mold line. No initial twist is prescribed, hence the initial design generates barely any lift. However, as pointed out in Sections A and B, the optimizer easily remedies this situation by pitching up the centerbody by only a few degrees.

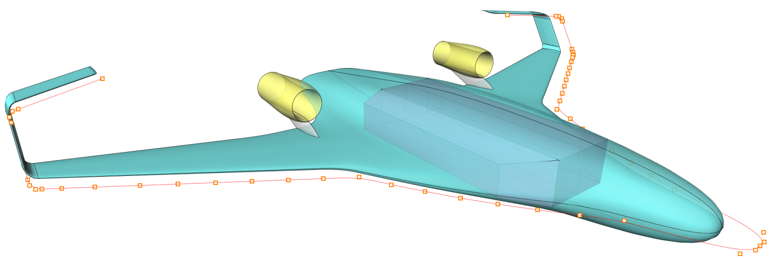

Figure 4: C-tip blended-wing-body regional jet. The axial curves are shown in red and their control points in orange.

Another appealing configuration is the box-wing: in theory, if the two wings are infinitely distanced, and each one carries half the lift of a monoplane of the same span, then the induced drag is halved. In practice, reductions on the order of 20% can be expected for vertical-gap-to-span ratios of about 0.1.[47] These results should also hold for swept wings in transonic flows by virtue of Munk's theorems, however in the high-subsonic regime several difficulties were uncovered by Lange et al. in 1974.[47] Chief among these was wing divergence encountered well below the target flutter speed. This problem was also well recognized by Frediani, whose solution was to mount the rear wings attaching at the tail on two vertical fins with maximum horizontal distance.[13] Although our models do not account for aeroelasticity, we still position the two fins on our design, see Figure 5, though like the fuselage we exclude them from the aerodynamic analyses. The airfoil selection here is of little importance since, as pointed by Wolkovitch,[48] the flow curvature induced by the neighboring wings calls for highly customized airfoils.

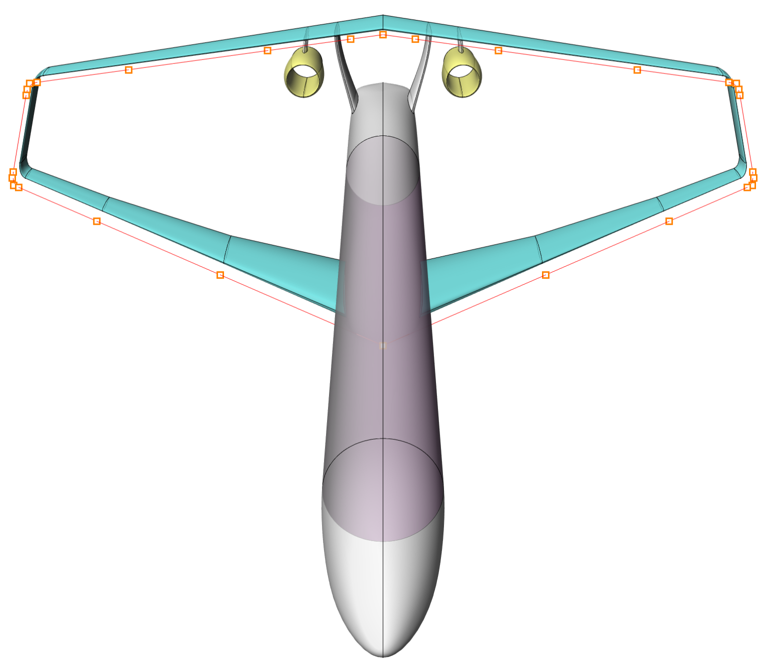

Figure 5: Box-wing regional jet. The axial curves are shown in red and their control points in orange.

The final aircraft configuration considered in this study is the strut-braced wing, which is similar to the truss-braced wing but without the additional juries. The strut is used for wing-bending load alleviation, thus allowing a higher aspect ratio wing with reduced thickness-to-chord ratios. The thinner wing has less transonic wave drag, permitting the wing to unsweep thus favoring natural laminar flow. We choose the planform and strut dimensions as per the guidelines of Jobe et al.,[49] resulting in a wingspan 1.5 times that of the baseline (see Figure 6 below). The main wing is based of the NASA SC(2)-0410 airfoil throughout its full span while the strut is interpolated from the NACA 64A-010 symmetric airfoil. Just like the previous three configurations, all wings are initially untwisted and have zero angles of incidence relative to the fuselage, i.e. the symmetry plane.

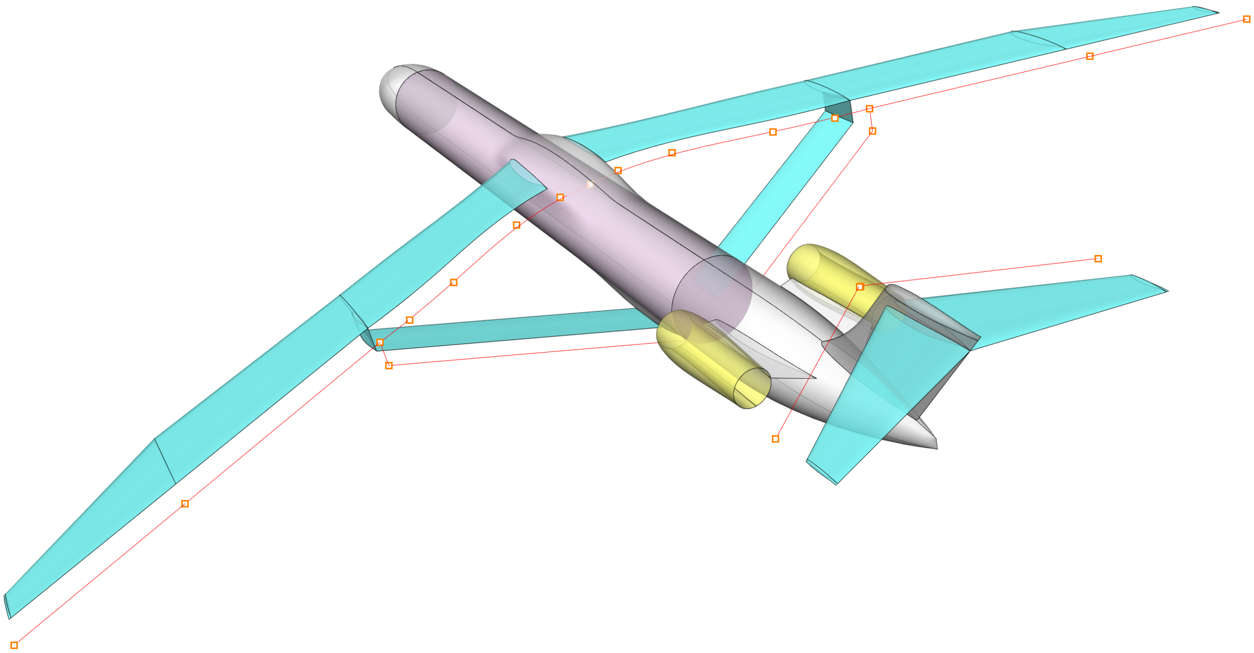

Figure 6: Strut-braced wing regional jet. The axial curves are shown in red and their control points in orange.

All four geometries were generated by an in-house drawing tool that is a hybrid between a script-based aircraft conceptual sketchpad and a CAD package.[24] Wing surfaces, including tails whenever applicable, (the cyan surfaces in Figures 3 to 6) were then output in IGES format and tesselated inside three-dimensional, multi-block meshes of H-H and O-grid topologies in ANSYS ICEM CFD. Some statistics are listed in Table 2 for the baseline grids used throughout the optimizations. The fine grids are obtained by refining, in parameter space, the final FFD block mappings responsible for the mesh movements, thus ensuring that the surface nodes coincide with the optimal shapes.

A. Span Efficiency Validations

Before considering optimization with practical constraints, we first present cases validating our new axial deformation approach. For each configuration, the optimizer is instructed to minimize drag while maintaining lift at zero angle-of-attack. Recall that the freestream Mach number is fixed at 0.78 for all cases. Since we are mainly interested in span efficiency, our approach to isolating induced drag is to eliminate wave drag by enabling section design variables. By further allowing twist variations, the optimizer should be able to recover span efficiencies equal to or greater than one by optimally loading all lifting surfaces. To avoid defining reference areas, we use the dimensional form of the span efficiency formula

$$e = \frac{L^2}{\pi q_\infty b^2 D_i}, \tag{5}$$

where L is the (constrained) lift, q_∞ the freestream dynamic pressure, b the span, and D_i the induced drag.

To prevent the wings from becoming excessively thin, we force, through a nonlinear constraint, the evolving wings to maintain at least 95% of their initial internal volume. We also restrict the vertical scaling

Design	Blocks	Grid sizes	Spacing	
			Off-wall	Wall[a]
Conventional tube-wing	126	2,461,956	0.000404	0.01242
	(2236)	(96,175,368)	(0.000109)	(0.00367)
C-tip blended-wing-body	234	1,646,820	0.000108	0.00521
	(2114)	(91,644,303)	(0.000027)	(0.00136)
Box-wing	96	1,893,570	0.000451	0.01390
	(2610)	(96,495,514)	(0.000118)	(0.00374)
Strut-braced wing	280	3,156,640	0.000608	0.02295
	(2206)	(92,712,289)	(0.000204)	(0.00751)

[a] $\sqrt{S/N_{\mathrm{wall}}}$, where S is the total surface area and N_{wall} the number of grids nodes on the wall surfaces.

Table 2: Grid size properties, in root-chord units, for each aircraft design. The numbers in parentheses refer to the refined grids.

factors, which are taken about the local origin of the FFD cross-sections (as explained in Section II), to be no less than 0.5 and no more than 1.5. This is with the exception of the cross-sections covering the centerbody of the blended-wing-body, for which we choose values of 0.95 and 1.05, respectively. As an aside, we warn the reader that enabling such sectional control often causes unavoidable explosions in the number of design variables. That is because we define each FFD cross-section with 10 chordwise control points, which translates to 20 section design variables (since there are 2 rows of control points in the vertical direction). While we recommend using at least 4 FFD cross-sections (80 section design variables) per wing segment, i.e. per axial curve, this number may be overly conservative in certain cases.

We begin with the conventional tube-wing baseline, for which the initial pressure contours are shown in Figure 7(a). Shocks are clearly seen on the aft region of the inboard upper wing and outboard along the leading edge. To remedy this, we start by defining three axial curves, two for the main wing and one for the horizontal tail, as illustrated in Figure 3. Note that on this figure, as well as on Figures 4 to 6, the axial curves have been translated for improved clarity; for the tube-wing, the axial curves are actually positioned at the leading edge of their respective wing segments, thus ensuring that the main wing's leading edge remains straight regardless of twist. There are 15 twist design variables and 300 section design variables (15 FFD cross-sections times 20 control points each), totaling 315 geometric design variables. The optimized wing is shown in Figure 7(b). Not only are the shocks completely eliminated, but the isobars are much more evenly spaced and at constant sweep angles. It is interesting to note that the optimal lift distribution inboard of the main wing does not appear to be elliptical in the presence of the lift-producing horizontal tail.

Next, inspecting Figure 8(a), we see that the initial blended-wing-body is mostly shock-free, except in the transonically stressed flow environment located inside the C-tip extension. This is emphasized in the top left inset, which reveals a complicated shock structure on the (not to-scale) inboard portion of the vertical fin. For the optimization, a total of 5 axial curves are used, visible in Figure 4: one going from the main body's root all the way to its tip, one for the vertical fin, one for the horizontal stabilizer, and two for the (smooth) corner transitions. Notice that many control points are required to capture the blended wing's leading edge. In our case, this approximation is exact since the axial curves are the same NURBS curves used to generate the blended-wing-body.[24] With a total of 29 twist and 580 section design variables, SNOPT reduced its optimality measure by 2 orders to 4.5×10^{-6} in 50 major iterations. The top view of the optimized surfaces, shown in Figure 8(b), indicates improved isobar tailoring, whereas the inset shows the now shock-free vertical portion.

Unlike the previous two cases, the initial flow solution of the box-wing configuration has no shock (due to the thin airfoils that could be selected because of its larger wing exposure) with the exception of a localized supersonic bubble at the leading edge root of the rear wing. Smooth flow gradients are also observed on the initial inboard portion of the vertical tip fin, shown in the top left corner of Figure 9(a). Indeed, unlike the blended-wing-body's C-tip, the flow there is not overly stressed by lateral disturbances caused by the presence of a highly tapered centerbody. To set up the optimization, we again use one axial curve per wing segment, plus two for the corner fillets, for a total of 7 axial curves. In all, there are 30 twist and 600 section design variables. Although the optimization converged by 2 orders and reduced overall drag by roughly 30%, the resulting spanwise lift distribution (Figure 9(b), right) is surprising. The optimizer almost completely unloaded the front wing by quite literally reversing its camber; hence, most of the lift is carried by the rear wing. This setting does form a favorable induced flow field for the (normally downwashed) rear wing, however this solution does not correspond to the global optimum. Indeed, as discussed in Section B, higher span efficiencies can be obtained when the two wings are encouraged to produce the same lift.

Just like the box-wing, the strut-braced wing has thin airfoil sections and as such sees no shock waves over most of its initial surfaces. The only detected shocks are found on the outboard panel of the strut intersecting the wing, although we choose to show the (not to-scale) inboard panel (Figure 10(a), top middle) for its more interesting flow patterns. Axial curves are assigned to wing segments in a similar fashion to the previous three cases, yielding 18 twist and 520 section design variables. The strut, being purely a structural member, is not allowed to twist and has limited freedom in sectional shape changes during the optimization. The optimizer takes 62 design cycles (67 function and gradient evaluations) to reduce optimality by 2 orders, from 1.7×10^{-2} to 1.6×10^{-4}. The flow on the optimized shape is remarkably well-behaved, as seen by the contours on Figure 10(b). Notice how the suction side of the strut is now reversed.

The span efficiencies of the above validation cases are summarized below in Table 3. These were calculated from a single flow solve performed on the fine grids of Table 2. The initial values are reported for comparison purposes only since they do account for nonzero wave drag.

	Conventional tube-wing	C-tip blended-wing-body	Box-wing	Strut-braced wing
Initial	0.8665	0.7706	0.8722	0.6536
Optimal	1.0169	1.2692	1.1349	0.9821

Table 3: Span efficiencies of the initial and optimally loaded designs.

B. Designs with Practical Constraints

Encouraged by the span efficiencies obtained, we repeat the same problems but now constrained by practical aircraft requirements. To begin with, each aircraft must perform the same mission: to carry 100 passengers and 3 crew members over 500 nm at Mach 0.78 and an altitude of 10.5 km ($\sim$ 35,000 ft). Since we limit ourselves to single-point optimizations, we pick the most critical point of the cruise segment, i.e. at the beginning where the required lift is maximum.

To estimate the aircraft weights, and therefore the required lift constraints at the specified altitude, we use a low-fidelity model based on wetted areas.[43] In this model, each major aircraft component is assigned a single weight per unit area, and that same value is used for all configurations. For example, the weight of the conventional tube-wing is reflected by the wetted areas of its “wing”, “tail”, “vertical”, and “fuselage” components. The same goes for the box-wing and strut-braced wing configurations. In the case of the blended-wing-body, only the “wing” component is used for the lack of a better weight estimate for the embedded fuselage. Although of limited accuracy, this approach at least ensures that each aircraft is sized according to the same technology levels. The values used in this work, listed in Table 4, are calibrated against the reported operating empty weight of the CRJ-1000.[45] The calibration assumes predetermined weights for the propulsion, equipment, operational, and useful load groups, all taken as percentages of the take-off gross weight of an aircraft of the same class.[43] Those weights are assumed fixed across all configurations.

Aside from the imposed lift constraint, we also add a y-directional moment constraint to each optimization problem for trimming purposes. We take the component-weighted centroids (based on the values in Table 4) as surrogates for centers of gravity. For the conventional tube-wing, this yields a center of gravity located at 29% of the mean aerodynamic chord (which suggests that the wings might have to be repositioned relative

Wing	Tail	Vertical	Fuselage
30.67	20.01	16.48	20.12

Table 4: Empty weight per wetted area [kg/m^2].

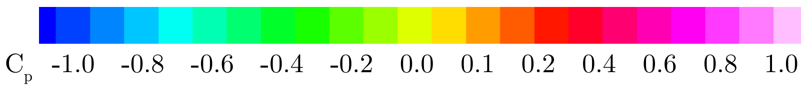

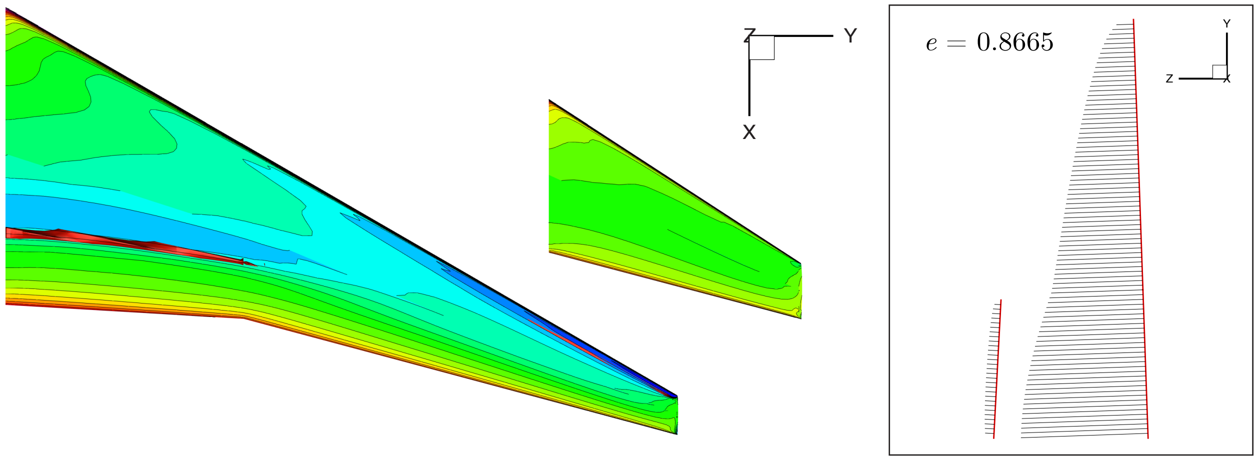

(a) Initial design. Shock surfaces are visible in dark red.

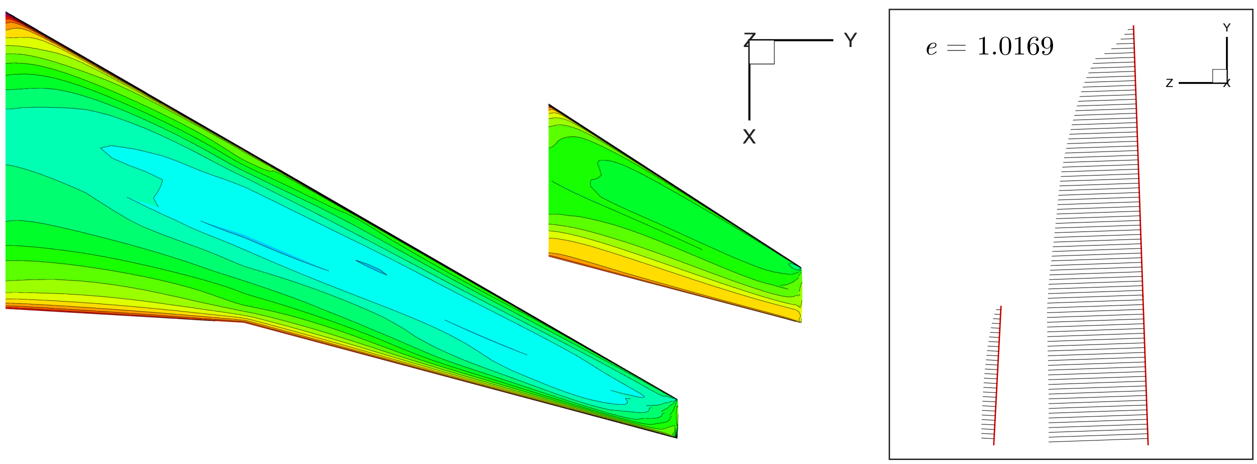

(b) Span efficiency validation.

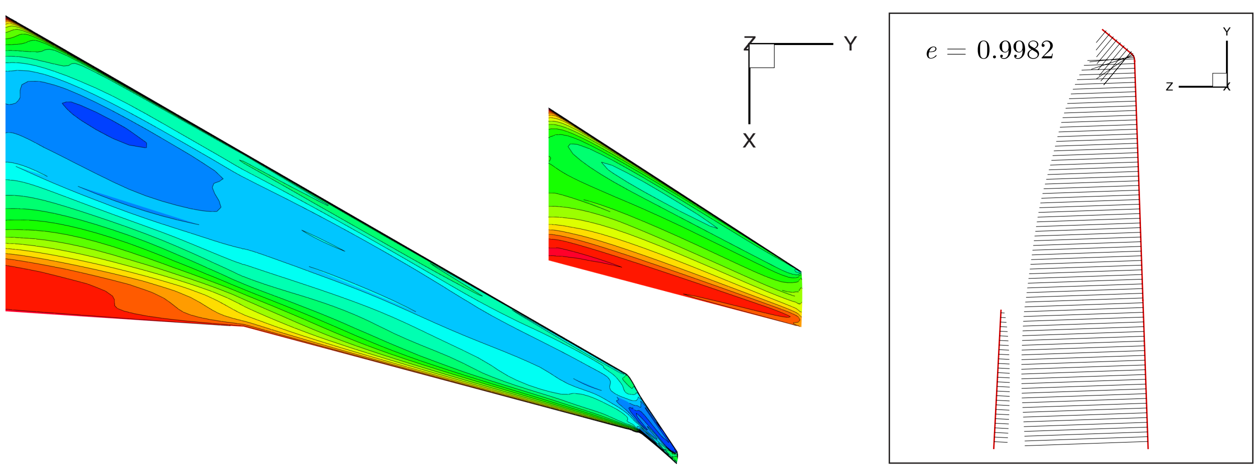

(c) Optimization with practical constraints.

Figure 7: Upper surface pressure coefficient contours (left) and spanwise lift/side force distribution (right) of the conventional tube-wing regional jet.

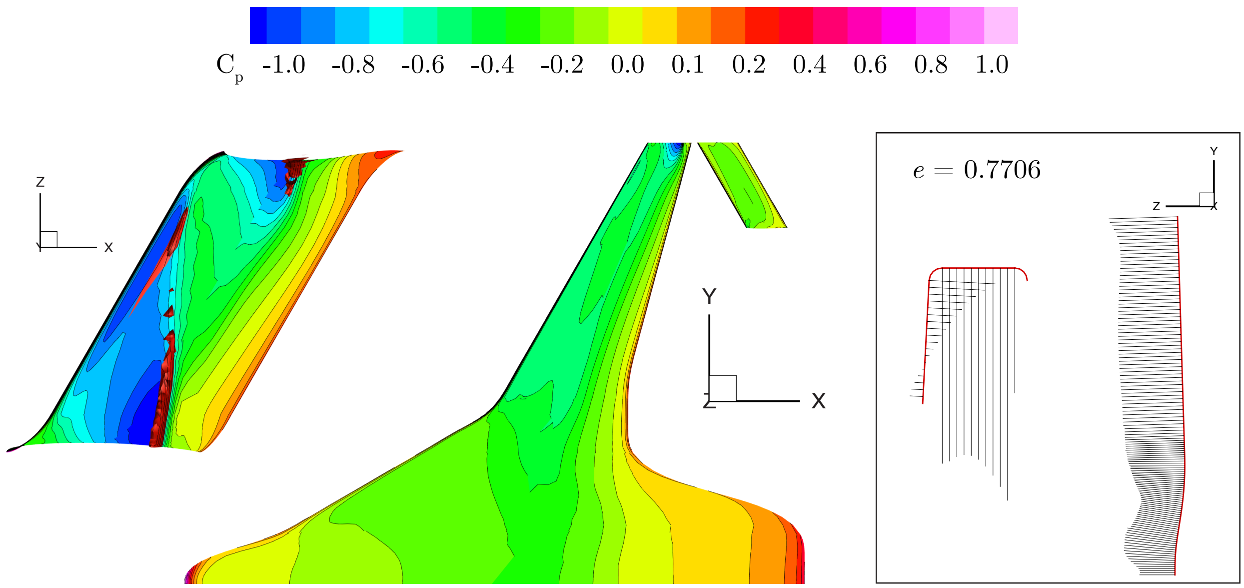

(a) Initial design. Shock surfaces are visible in dark red.

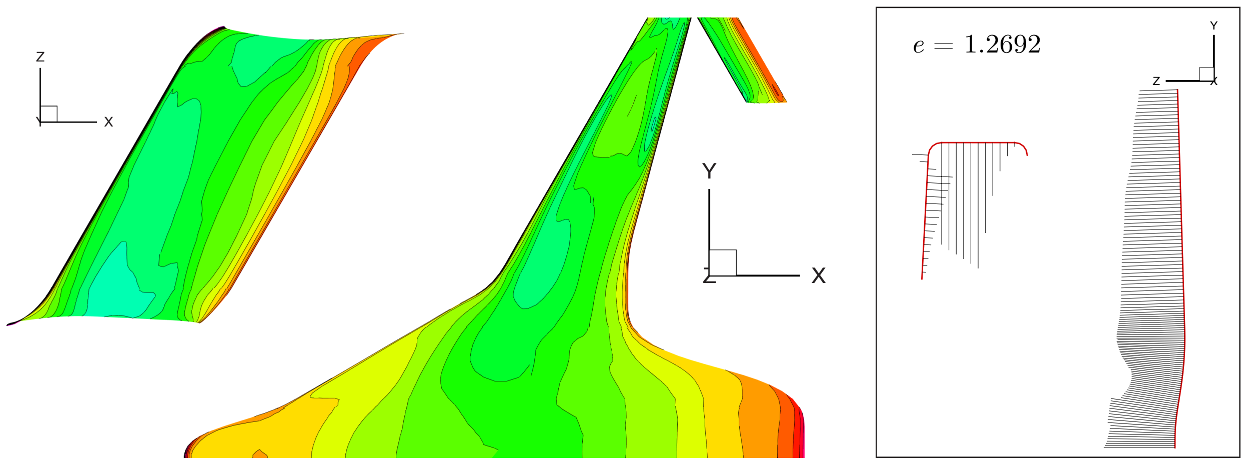

(b) Span efficiency validation.

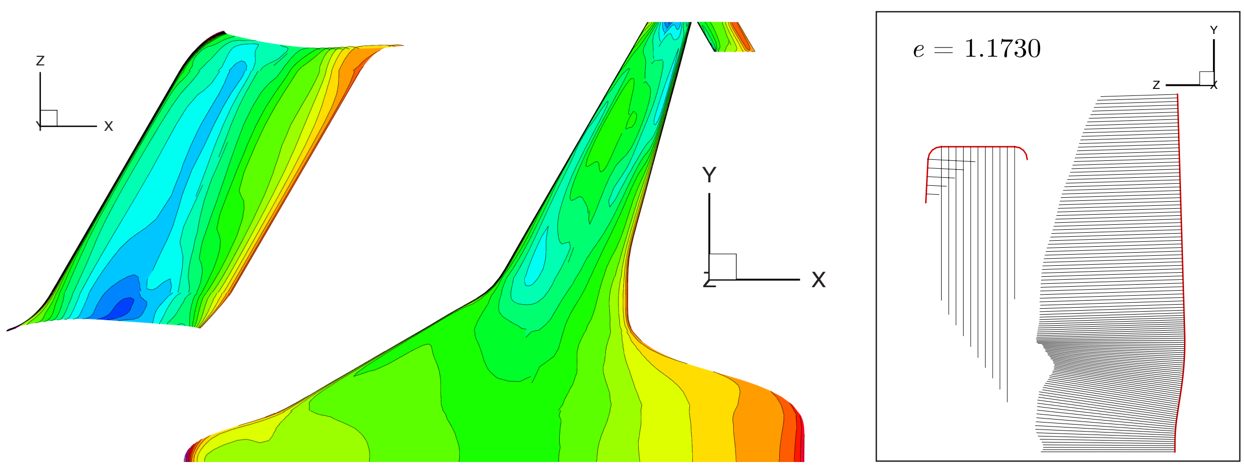

(c) Optimization with practical constraints.

Figure 8: Upper surface pressure coefficient contours (left) and spanwise lift/side force distribution (right) of the C-tip blended-wing-body regional jet. Top left insets: inboard panel of the vertical tip fin.

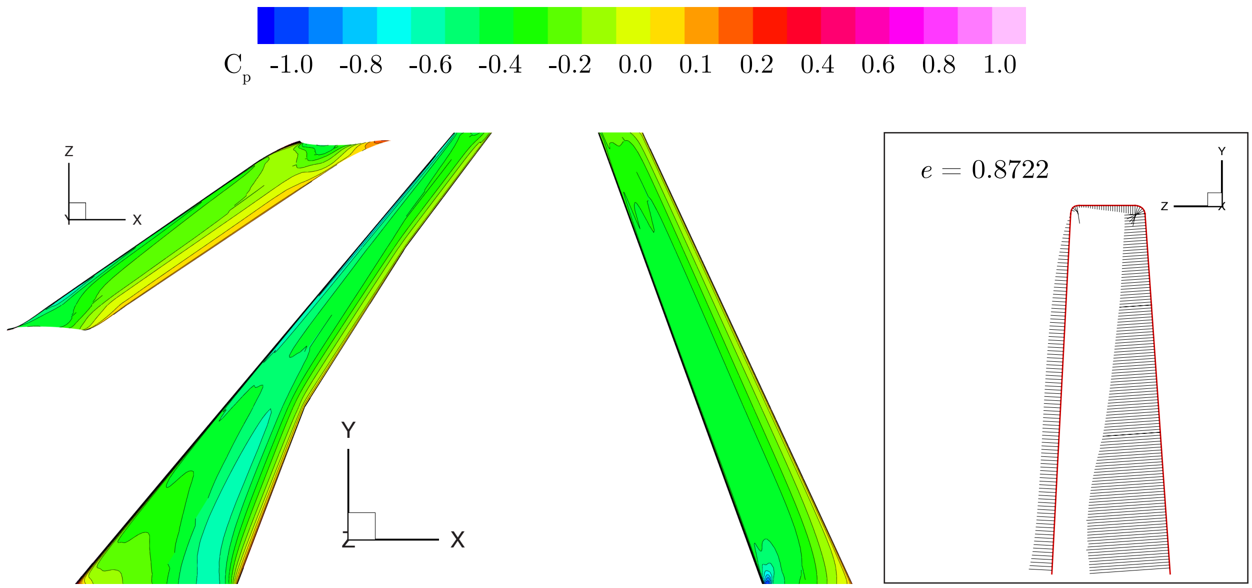

(a) Initial design.

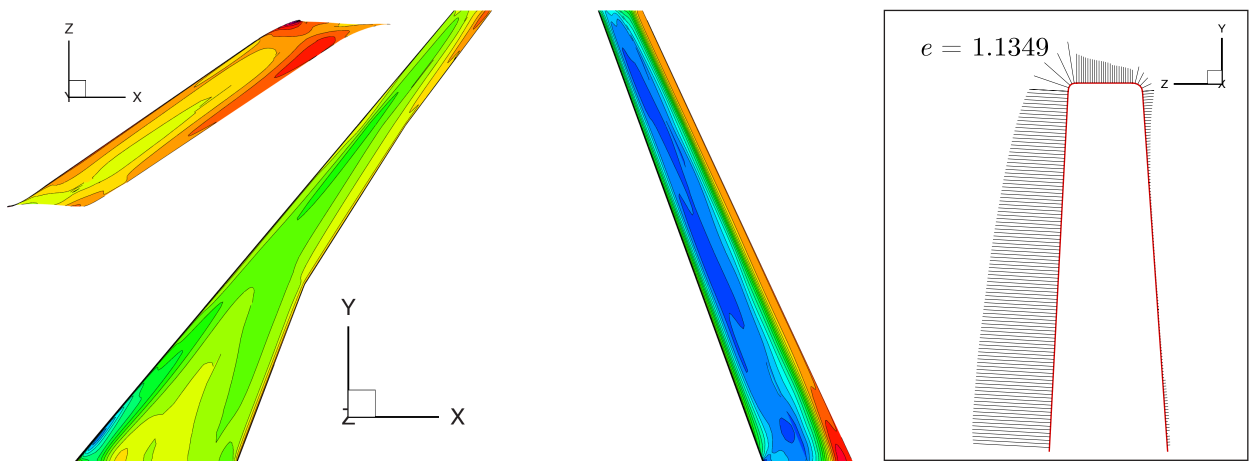

(b) Span efficiency validation.

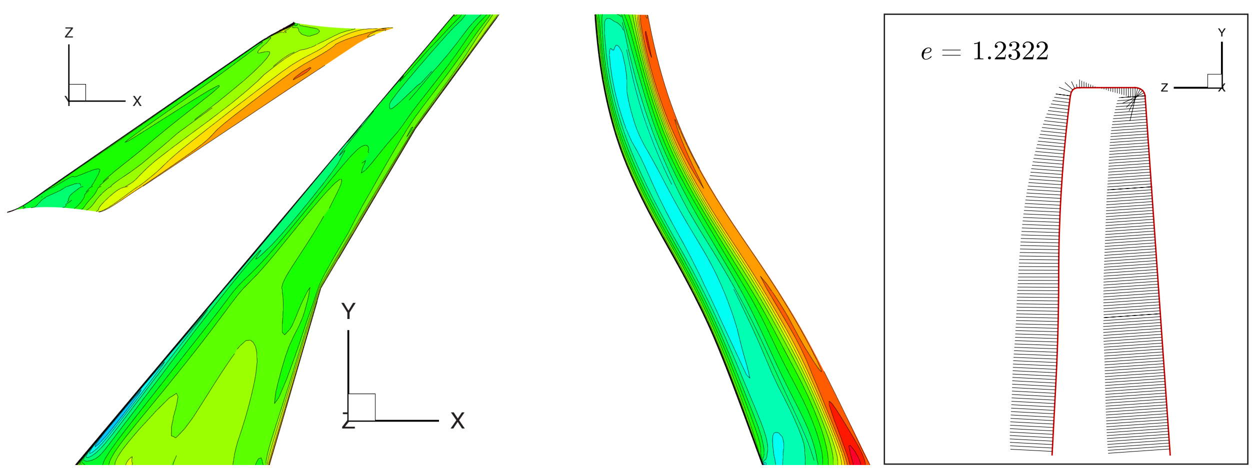

(c) Optimization with practical constraints.

Figure 9: Upper surface pressure coefficient contours (left) and spanwise lift/side force distribution (right) of the box-wing regional jet. Top left insets: inboard panel of the vertical tip fin.

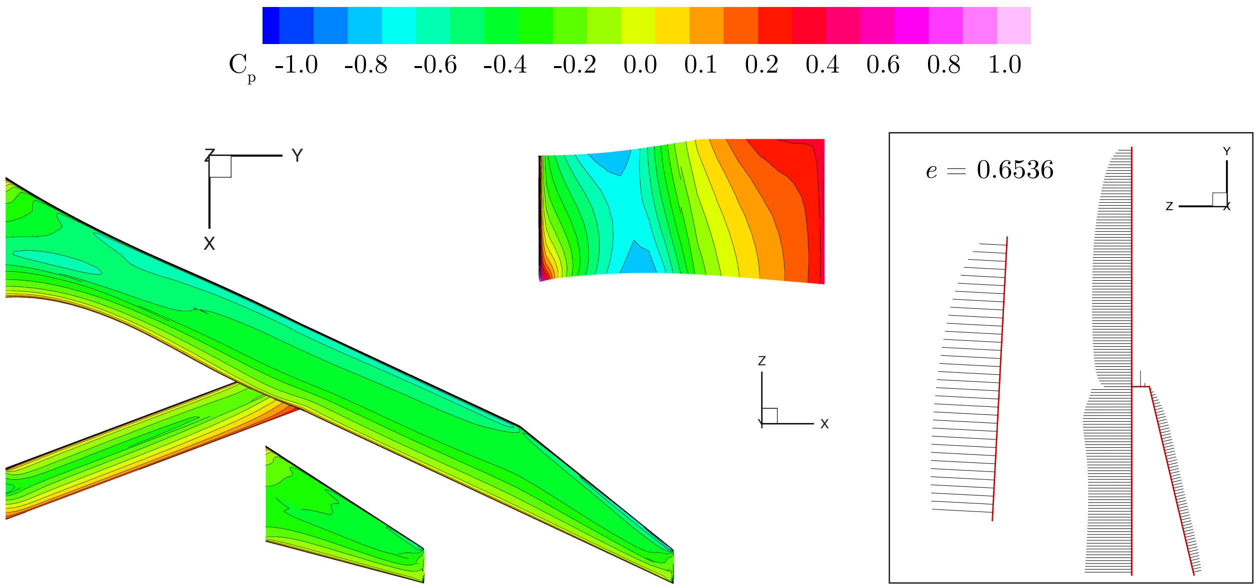

(a) Initial design.

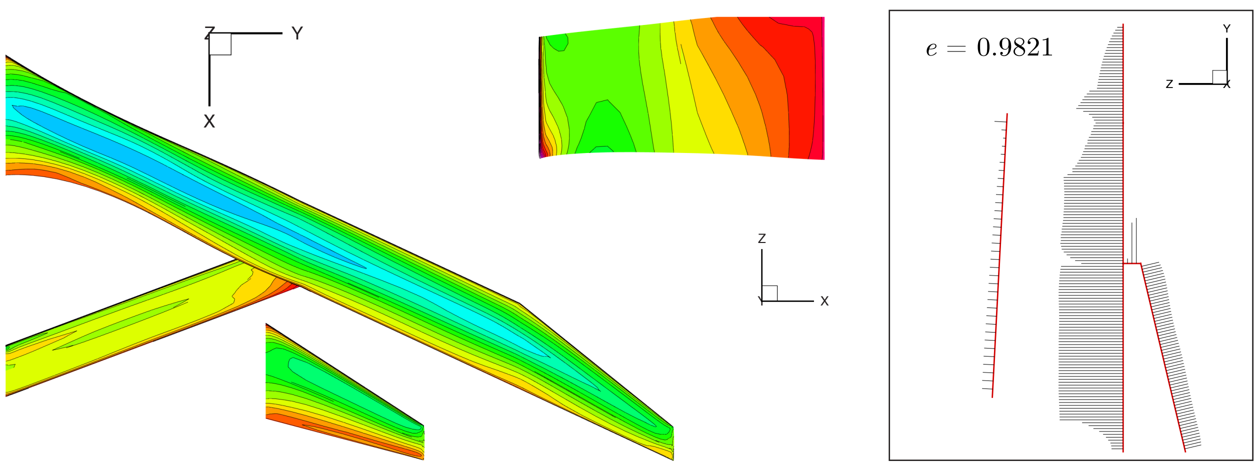

(b) Span efficiency validation.

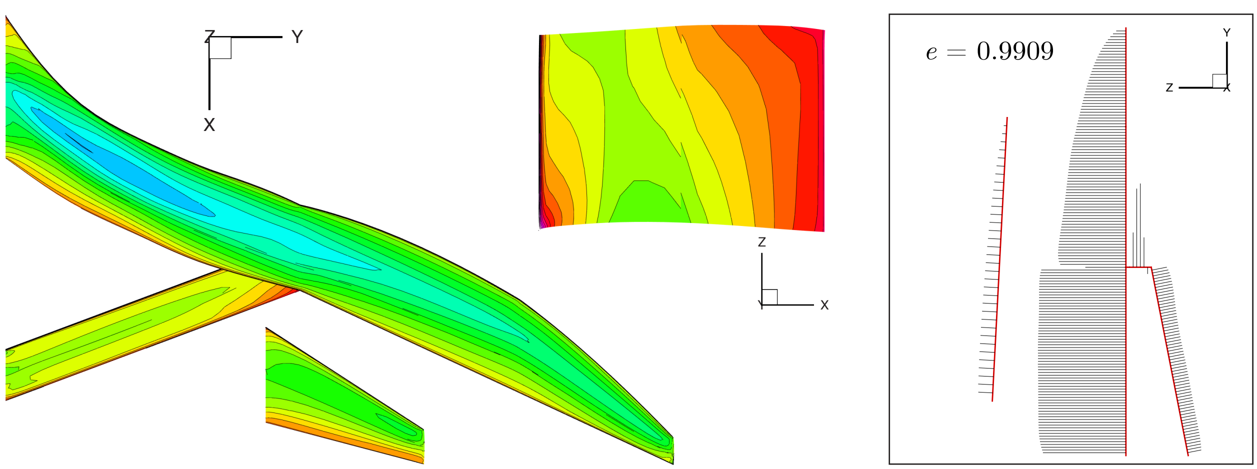

(c) Optimization with practical constraints.

Figure 10: Upper surface pressure coefficient contours (left) and spanwise lift/side force distribution (right) of the strut-braced wing regional jet. Top middle insets: inboard panel of the vertical strut.

to the fuselage, but such action was deemed unnecessary given the lack of a stability criterion in our models). The same goes for the unconventional aircraft, but, in order to account for their greater overall uncertainty in say, wing planform, the longitudinal position of their center of gravity is considered a design variable, with a margin with respect to the centroid of plus or minus 3% of the fuselage length.

We reuse the same axial curve/FFD volume combinations as in Section A, but this time we free up some of the axial curves' control points with the goal of exploring the design space of each configuration. Depending on the configuration at hand, we try to do so in a manner that is sensible both from an aerodynamic and a structural point of view. For example, for the conventional wing only, we allow a winglet to grow (to help it compete with the unconventional designs), but we heavily restrict the winglet's taper (to help reduce the root bending moment). In general, because there is no structural model involved, we allow neither wing span nor wing sweep to vary during any of the optimizations.

Let us begin with the conventional tube-wing. As just pointed out, we provide the optimizer the means to produce a winglet. This is achieved by replacing the outer axial curve, visible in Figure 3, with three other axial curves attached one after another, as seen in Figure 11. The axial curve that is sandwiched is cubic and is specifically defined to reproduce Bombardier's signature "beaver tail". That same axial curve also provides a smooth wing-winglet transition together with the outermost axial curve, whose end point controls the vertical extent of the winglet. As expected, at the end of the simulation the optimizer reaches the upper bound of that vertical height. For comparison, we reran the exact same optimization problem but without that permissible vertical extent (that is, with 1 less degree of freedom), and we found that the winglet-up configuration produces roughly 3.5% less drag. As seen from Figure 7(c), the optimized wing is optimally loaded even though it carries significantly more lift. Some of this extra lift come as a consequence of the negative force exercised on the tail to trim the aircraft. In fact, where there used to be a dip in the spanwise force distribution of the main wing is now a bulge.

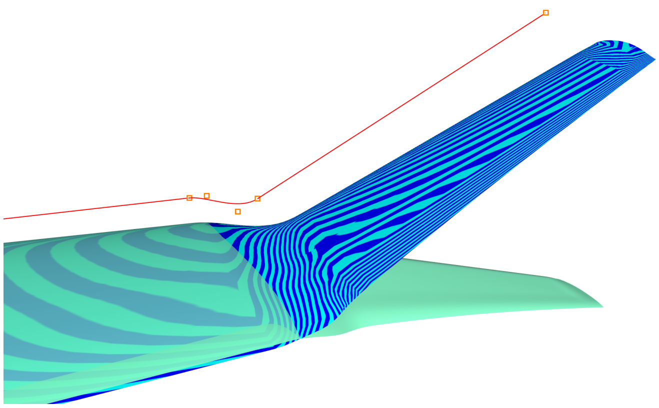

Figure 11: Close-up of the optimized tip geometries. Both solutions exhibit wavy surfaces toward the trailing edge, as seen by the jump in the zebra curvature stripes on the winglet-up configuration.

We now shift our attention to the blended-wing-body, which is, in a sense, doubly unconventional with its C-tip extension. Unlike their planar counterparts, the aerodynamics of C-tip blended-wing-bodies have not received much attention in the past. Hence, we focus our efforts on the C-tip extension, more specifically on its top horizontal segment. Originally, we varied both its length and dihedral angle, only to realize that the optimizer invariably tried to eliminate it in favor of a higher vertical winglet, i.e. it wanted to "unfold" the C shape. We say "tried" because the optimizer's attempts were ultimately curtailed by mesh movement failures. We thus took a step back and varied the horizontal segment's spanwise extent only. As seen from the resulting planform in Figure 8(c), the optimizer still chose to reduce this value as much as it could (by the end of the optimization the lower bound is active). This suggests that for a fixed height to vertical gap ratio, the C-tip is not advantageous — perhaps even disadvantageous — over the purely vertical winglet. Though surprising, a similar conclusion was reached by Verstraeten and Slingerland when comparing optimally loaded wingletted and C wings.[50] As for the final twist angle of the centerbody's root section, the optimizer naturally reaches 2.15 degrees, thus favoring a reasonable deck angle at cruise.

Next in line is the box-wing. Recall from Section A and Figure 9(b) that the optimizer elected to transfer most of the lift onto the rear wing. Maybe the optimizer did find a true local optimum, but we believe that it more likely exploited numerical artifacts arising from the somewhat coarse discretization of our grid. After all, classical lifting-line theory clearly indicates that both wings should generate equal lift for minimum induced drag.[47] In terms of aircraft trim, this necessarily implies that the center of gravity must lie midway between the front and rear wings, a fact that was unaccounted for at the conceptual design stage of this work. Thus, for the box-wing only, we disregard the fuselage weight and place the center of gravity based on the centroids of the front and rear wings only. Also, using a quadratic axial curve, we give the optimizer some freedom in shaping the outboard portion of the rear wing's planform while ensuring that the location where the vertical fin intersects remains unchanged. Finally, linear taper variations are activated on all wing segments, thus giving the optimizer the opportunity to redistribute internal volume between the front and rear wings. As portrayed in Figure 9(c), the optimal solution exhibits almost equally loaded wings. Indeed, the spanwise lift distribution closely resembles the one found by Prandtl in 1924: elliptical on both wings and joined at the tip by a butterfly-shaped side-force distribution.[11]

The final case considered is the strut-braced wing, for which we further relax the axial curves' range of potential deformation. First, similar to the box-wing design, we activate the chordwise scaling variables (taper) along the main wing, but this time we allow nonlinear changes. Because the axial curves are positioned on the wing's trailing edge, the latter will remain straight as taper is varied. Second, the first four axial curve's points controlling the inboard wing segment (of which the very first appears inside the fuselage in Figure 6) are free to move in the chordwise direction by plus or minus 0.2 root-chord units. Hence, for this region only the curvature of the trailing edge can potentially vary. Finally, the height of the vertical strut segment is also subjected to change by plus or minus 0.1 root-chord units. At the end of the optimization, the optimizer reaches the lower bound of that last design variable, thus maximizing the vertical gap between the wing and the horizontal strut segment. This relieves the flow passing through the wing-strut opening. Also, visible in Figure 10(c) and of higher interest is the final planform. The initial kink at about 80% span appears to disappear, blended by a smooth bird-like leading edge. The inboard wing is also curved, but in such a way to maximize the root sweep angle so to delay isobar unsweeping at the symmetry plane.

A summary of the results obtained from the optimizations just described is tabulated below. The aircraft weights at the beginning of cruise are also included. It is interesting to note how the optimized box-wing's span efficiency is now 1.2322, in good agreement with the expected value of about 1.2 that corresponds to a vertical gap to span ratio ratio, h/b, of 0.1.[47] The last line of Table 5 offers a comparison in terms of induced drag reduction between the conventional configuration and the unconventional ones. According to this preliminary study on regional transports, the strut-braced wing concept is the one that generates the least amount of induced drag (−46%), followed by the C-tip blended-wing-body (−28%), and finally the box-wing aircraft (−9%).

	Conventional tube-wing	C-tip blended-wing-body	Box-wing	Strut-braced wing
e	0.9982	1.1730	1.2322	0.9909
Lift/Drag	55.5	84.3	64.9	110.0
Weight [N]	370,068	407,321	395,099	397,336
Drag [N]	6,668	4,832	6,088	3,612
ΔDrag [%]	0	28	9	46

Table 5: Performance and drag reduction of the optimized practical designs.

V. Conclusions

This paper introduced an intuitive and versatile technique that parameterizes wing shape changes. It uses the principles of axial deformation combined with those of free-form deformation to achieve both global and local control. Any form of span, sweep, dihedral, taper, twist, and sectional shape changes can be achieved by the means of simple transformation matrices, an approach that promotes an easy and thorough exploration of the design space. The technique also proved to be directly extensible to multi-segmented wings of arbitrary topology. Together these characteristics are advantageous in the systematic and consistent study of unconventional lifting systems.

The second portion of this work sought to assess and quantify the relative aerodynamic benefits of three next-generation unconventional regional jets compared with a conventional baseline aircraft sized for the same mission. From a purely induced drag perspective, our results indicate that the strut-braced wing configuration is the most efficient. This is assuming that the strut does indeed allow for a span 1.5 times that of the conventional baseline (even if it does not, additional trusses could presumably help relieve stress paths). The poorer performance of the box-wing should not by any means deter further investigation. Indeed, if the vertical gap to span ratio were to double, i.e. taken from 0.1 to 0.2, drag reductions on the order of 21% can be expected.

Two secondary outcomes of the optimizations are worth reiterating. The first is that a box-wing is optimally loaded only when the front and rear wings carry the same amount of lift, which entails that the center of gravity should be halfway between the two wings. This observation could only be made possible with sufficiently fine mesh spacings, fine enough to capture the many subtleties present in the induced flow field generated by the staggered wings. The second point is that a C wing does not appear to offer any drag benefit over a vertical winglet of the same height to span ratio. Either this trend represents a real phenomenon, or, similar to the box-wing, our grid was simply too coarse to capture the real physics. More work is needed to elucidate this dilemma.

This paper only marks the beginning in assessing the real potential of unconventional aircraft for commercial aviation. It remains to be determined whether viscous effects negate savings in induced drag. For instance, a 2011 NASA contractor report reveals that the only way to achieve a 30% reduction in induced and parasitic drag (along with a 30% improvement in vehicle weight and engine fuel consumption) for the 2035 timeframe is to substantially reduce wetted area, such as could be achieved by a tailless airliner.[51] This report goes to show the unusually strong coupling between the many disciplines involved in the design of unconventional aircraft; hence future work will not only address viscous effects but also include structural models culminating in high-fidelity multi-point aerostructural optimizations.

Acknowledgments

We are thankful for the financial support provided by the Ontario Graduate Scholarship (OGS) in conjunction with the University of Toronto. Computations were performed on the gpc supercomputer at the SciNet HPC Consortium.

References

[1]Green, J. E., "Civil aviation and the environment - the next frontier for the aerodynamicist," *The Aeronautical Journal*, Vol. 110, No. 1110, August 2006, pp. 469–486.

[2]Collier, F., "Overview of NASA's Environmentally Responsible Aviation (ERA) Project," *48th AIAA Aerospace Sciences Meeting*, Orlando, Florida, January 2010.

[3]Kroo, I. M., "Drag due to lift: concepts for prediction and reduction," *Annual Review of Fluid Mechanics*, Vol. 33, No. 1, January 2001, pp. 587–617.

[4]Munk, M. M., "The Minimum Induced Drag of Aerofoils," Tech. Rep. 121, National Advisory Committee for Aeronautics, 1921.

[5]Mangler, W., "The Lift Distribution of Wings with End Plates," Tech. Rep. 856, National Advisory Committee for Aeronautics, 1938.

[6]Cone, C. D. J., "The Theory of Induced Lift and Minimum Induced Drag of Nonplanar Lifting Systems," Tech. Rep. 139, National Aeronautics and Space Administration, 1962.

[7]Kroo, I. M., "Nonplanar Wing Concepts for Increased Aircraft Efficiency," *VKI Lecture Series on Innovation Configurations and Advanced Concepts for Future Civil Aircraft*, Rhode-St-Genese, Belgium, June 2005.

[8]Whitcomb, R., "Research on Methods for Reducing the Aerodynamic Drag at Transonic Speeds," *Inaugural Eastman Jacobs Lecture*, NASA Langley Research Center, November 1994.

[9]Bushnell, D., "Aircraft drag reduction — a review," *Proceedings of the Institution of Mechanical Engineers, Part G: Journal of Aerospace Engineering*, Vol. 217, No. 1, January 2003, pp. 1–18.

[10]Torenbeek, E. and Deconinck, H., editors, *Innovative configurations and advanced concepts for future civil transport aircraft*. von Karman Institute for Fluid Dynamics, June 2005.

[11]Prandtl, L., "Induced Drag of Multiplanes," Tech. Rep. 182, National Advisory Committee for Aeronautics, 1924.

[12]Miranda, L. R., "Boxplane Configuration — Conceptual Analysis and Initial Experimental Verification," Tech. Rep. 25180, Lockheed-California Company, 1972.

[13]Frediani, A., "The Prandtl wing," *Innovative configurations and advanced concepts for future civil transport aircraft*, edited by E. Torenbeek and H. Deconinck, von Karman Institute for Fluid Dynamics, June 5–10 2005.

[14]Liebeck, R. H., "Design of the Blended Wing Body Subsonic Transport," *Journal of Aircraft*, Vol. 41, No. 1, January-February 2004, pp. 10–25.

[15]Pfenninger, W., "Laminar Flow Control Laminarization," Tech. Rep. 654, Advisory Group for Aerospace Research and Development, 1976.

[16]Gur, O., Schetz, J. A., and Mason, W. H., "Aerodynamic Considerations in the Design of Truss-Braced-Wing Aircraft," *Journal of Aircraft*, Vol. 48, No. 3, May-June 2011, pp. 919–939.

[17]Lange, R. H., "Review of Unconventional Aircraft Design Concepts," *Journal of Aircraft*, Vol. 25, No. 5, May 1988, pp. 385–392.

[18]Schmitt, D., "Challenges for unconventional transport aircraft configurations," *Air & Space Europe*, Vol. 3, No. 3–4, 2001, pp. 67–72.

[19]Kehayas, N., “Aeronautical technology for future subsonic civil transport aircraft,” *Aircraft Engineering and Aerospace Technology: An International Journal (January 2007)*, Vol. 79, No. 6, January 2007, pp. 600–610.

[20]Qin, N., Vavalle, A., Le Moigne, A., Laban, M., Hackett, K., and Weinerfelt, P., “Aerodynamic considerations of blended wing body aircraft,” *Progress in Aerospace Sciences*, Vol. 40, No. 6, August 2004, pp. 321–343.

[21]Qin, N., Vavalle, A., and Le Moigne, A., “Spanwise Lift Distribution for Blended Wing Body Aircraft,” *Journal of Aircraft*, Vol. 42, No. 2, March-April 2005, pp. 356–365.

[22]Lyu, Z. and Martins, J. R. R. A., “Aerodynamic Shape Optimization of a Blended-Wing-Body Aircraft,” *51st AIAA Aerospace Sciences Meeting,* AIAA Paper 2013-0283, Grapevine, Texas, January 2013.

[23]Reist, T. A. and Zingg, D. W., “Aerodynamic Shape Optimization of a Blended-Wing-Body Regional Transport for a Short Range Mission,” *21st AIAA Computational Fluid Dynamics Conference,* AIAA Paper 2012-2414, San Diego, California, June 2013.

[24]Gagnon, H. and Zingg, D. W., “Geometry Generation of Complex Unconventional Aircraft with Application to High-Fidelity Aerodynamic Shape Optimization,” *21st AIAA Computational Fluid Dynamics Conference,* AIAA Paper 2013-2850, San Diego, California, June 2013.

[25]Ning, S. A. and Kroo, I., “Tip Extensions, Winglets, and C-wings: Conceptual Design and Optimization,” *28th AIAA Applied Aerodynamics Conference,* AIAA Paper 2008-7052, Honolulu, Hawaii, August 2008.

[26]Jansen, P. W., Perez, R. E., and Martins, J. R. R. A., “Aerostructural Optimization of Nonplanar Lifting Surfaces,” *Journal of Aircraft*, Vol. 47, No. 5, 2010, pp. 1490–1503.

[27]Anderson, G. R., Aftosmis, M. J., and Nemec, M., “Parametric Deformation of Discrete Geometry for Aerodynamic Shape Design,” *50th AIAA Aerospace Sciences Meeting,* AIAA Paper 2012-0965, Nashville, Tennessee, January 2012.

[28]Gagnon, H. and Zingg, D. W., “Two-Level Free-Form Deformation for High-Fidelity Aerodynamic Shape Optimization,” *14th AIAA/ISSMO Multidisciplinary Analysis and Optimization Conference,* AIAA Paper 2012-5447, Indianapolis, Indiana, September 2012.

[29]Fudge, D., Zingg, D. W., and Haimes, R., “A CAD-Free and a CAD-Based Geometry Control System for Aerodynamic Shape Optimization,” *43rd AIAA Aerospace Sciences Meeting,* AIAA Paper 2005-0451, Reno, Nevada, January 2005.

[30]Sederberg, T. W. and Parry, S. R., “Free-Form Deformation of Solid Geometric Models,” *Proceedings of the 13th Annual Conference on Computer Graphics and Interactive Techniques*, Dallas, Texas, August 1986.

[31]Lazarus, F., Coquillart, S., and Jancène, P., “Axial deformations: an intuitive deformation technique,” *Computer-Aided Design*, Vol. 26, No. 8, 1994, pp. 607–613.

[32]Gain, J. and Bechmann, D., “A Survey of Spatial Deformation from a User-Centered Perspective,” *ACM Transactions of Graphics*, Vol. 27, No. 4, 2008, pp. 107:1–107:21.

[33]Piegl, L. A., “On NURBS: a survey,” *Computer Graphics and Applications*, Vol. 11, No. 1, 1991, pp. 55–71.

[34]Goldman, R., *Matrices and Transformations,* Graphics Gems I, Academic Press, 1990.

[35]Goldman, R., *More Matrices and Transformations: Shear and Pseudo-Perspective,* Graphics Gems II, Academic Press, 1991.

[36]Hicken, J. E. and Zingg, D. W., “Aerodynamic Optimization Algorithm with Integrated Geometry Parameterization and Mesh Movement,” *AIAA Journal*, Vol. 48, No. 2, February 2010, pp. 400–413.

[37]Strand, B., “Summation by parts for finite difference approximations for d/dx,” *Journal of Computational Physics*, Vol. 110, No. 1, January 1994, pp. 47–67.

[38]Carpenter, M. H., Gottlieb, D., and Abarbanel, S., “Time-stable boundary conditions for finite-difference schemes solving hyperbolic systems: methodology and application to high-order compact schemes,” *Journal of Computational Physics*, Vol. 111, No. 2, April 1994, pp. 220–236.

[39]Hicken, J. E. and Zingg, D. W., “Parallel Newton-Krylov Solver for the Euler Equations Discretized Using Simultaneous-Approximation Terms,” *AIAA Journal*, Vol. 46, No. 11, November 2008, pp. 2273–2786.

[40]Gill, P. E., Murray, W., and Saunders, M. A., “SNOPT: An SQP Algorithm for Large-Scale Constrained Optimization,” *SIAM Review*, Vol. 47, No. 1, 2005, pp. 99–131.

[41]Nocedal, J. and Wright, S. J., *Numerical Optimization*, Springer, 2nd ed., 2006.

[42]Squire, W. and Trapp, G., “Using Complex Variables to Estimate Derivatives of Real Functions,” *SIAM Review*, Vol. 40, No. 1, March 1998, pp. 110–112.

[43]Raymer, D. P., *Aircraft Design: A Conceptual Approach*, American Institute of Aeronautics and Astronautics, Blacksburg, Virginia, 4th ed., 2006.

[44]Harris, C. D., “NASA Supercritical Airfoils,” Tech. Rep. Paper 2969, National Aeronautics and Space Administration, Hampton, Virginia, 1990.

[45]Bombardier Inc., “Results speak,” [http://www.crjnextgen.com, accessed 09/12/13].

[46]Kafyeke, F., Pépin, F., and Kho, C., “Development of High-Lift Systems for the Bombardier CRJ-700,” *23rd International Congress of the Aeronautical Sciences*, Toronto, Ontario, September 2002.

[47]Lange, R. H., Cahill, J. F., Bradley, E. S., Eudaily, R. R., Jenness, C. M., and MacWilkinson, D. G., “Feasibility Study of the Transonic Biplane Concept for Transport Aircraft Application,” Tech. Rep. 132462, National Aeronautics and Space Administration, 1974.

[48]Wolkovitch, J., “The Joined Wing: An Overview,” *Journal of Aircraft*, Vol. 23, No. 3, March 1986, pp. 161–178.

[49]Jobe, C. E., Kulfan, R. M., and Vachal, J. D., “Wing Planforms for Large Military Transports,” *Journal of Aircraft*, Vol. 16, No. 7, July 1979, pp. 425–432.

[50]Verstraeten, J. G. and Slingerland, R., “Drag Characteristics for Optimally Span-Loaded Planar, Wingletted, and C Wings,” *Journal of Aircraft*, Vol. 46, No. 3, May-June 2009, pp. 962–971.

[51]Raymer, D. P., Wilson, J., Douglas Perkins, H., Rizzi, A., Zhang, M., and Ramirez Puentes, A., “Advanced Technology Subsonic Transport Study,” Tech. Rep. 217130, National Aeronautics and Space Administration, Cleveland, Ohio, 2011.

A. General Arrangement of the Initial Designs

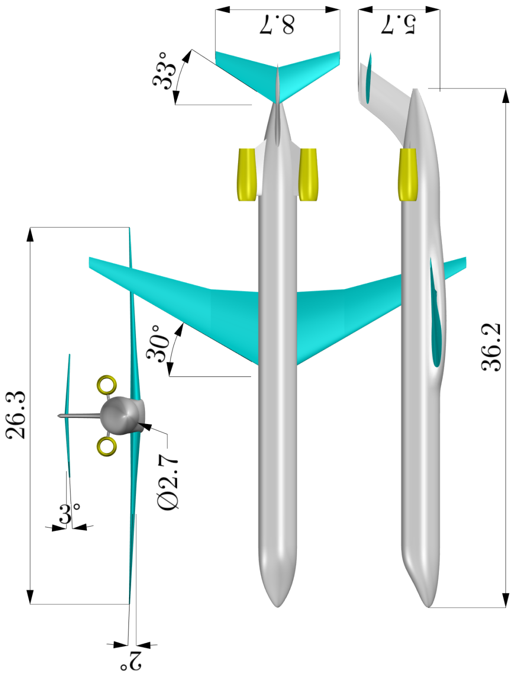

(a) Conventional tube-wing

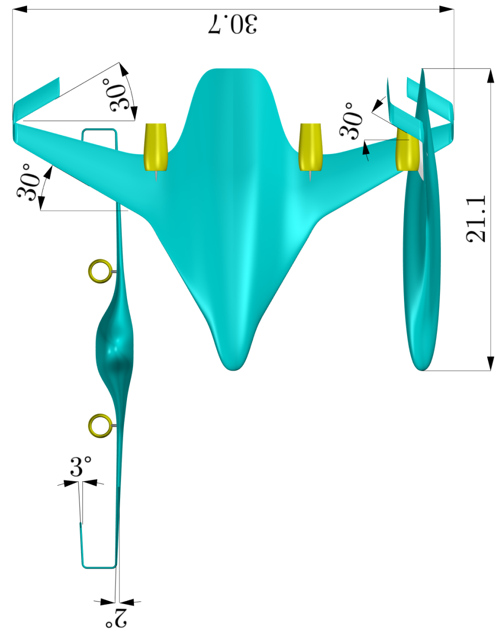

(b) C-tip blended-wing-body

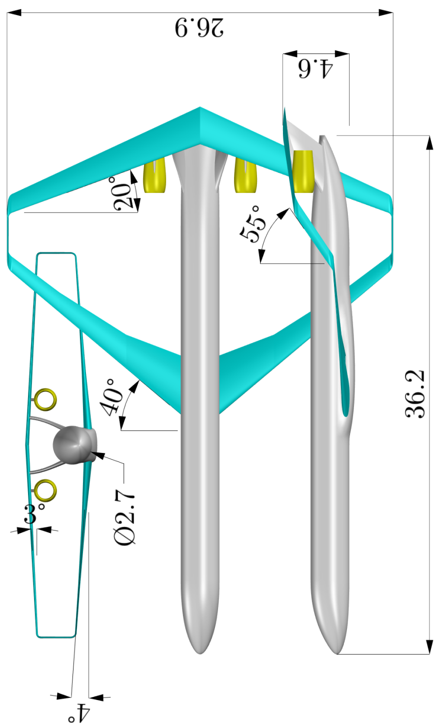

(c) Box-wing

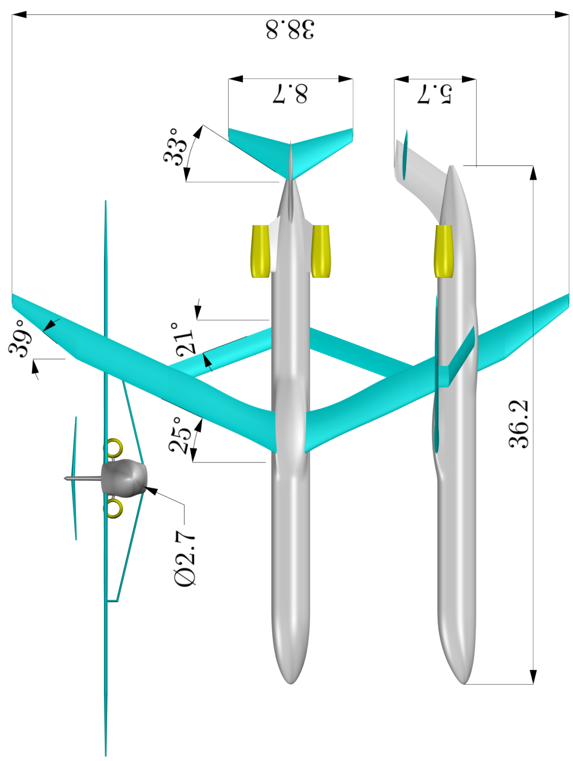

(d) Strut-braced wing

Figure 12: Overall dimensions (in meters) of the initial designs. Drawings are to scale relative to each other.